An Analysis on the Flow Field Structures and the Aerodynamic Noise of Airfoils with Serrated Trailing Edges Based on Embedded Large Eddy Flow Simulations

Z. Zuo[†], Q. Huang and S. Liu

State Key Laboratory of Hydroscience and Engineering Laboratory, Department of Energy and Power Engineering, Tsinghua University, Beijing, Beijing, 100084, China

†*Corresponding Author Email: zhigangzuo200@mail.tsinghua.edu.cn*

ABSTRACT

This paper presents the numerical analysis on the aerodynamic flows and noise of airfoils with serrated trailing edges at $Re=1.6\times10^5$. Flow simulations were performed with an embedded large eddy simulation (ELES) method. Two modified airfoils with serrated trailing edges (same widths, different lengths) were studied and compared with the baseline airfoil baseline NACA-0018 airfoil. It is seen that the unsteady lift and drag coefficients of the baseline airfoil A0 have a peak at about 2270Hz, which is close to the tonal noise frequency experimentally observed. Under the flow conditions studied in this research, the longer saw tooth serrations changed the flow fields near the trailing edge, which provides the potential of suppressing the tonal noise. Predictions based on acoustic analogy indicate that the longer saw tooth serrations decreases the overall sound pressure levels. This paper provides a basic understanding of the noise reduction mechanism in the airfoils with serrated trailing edges.

Keywords: Aerodynamic noise; Airfoil; Serrated trailing edge; Embedded Large Eddy Simulation (ELES); Numerical simulation.

NOMENCLATURE

C	airfoil chord	St	Strouhal number
C_D	drag coefficient	T_u	streamwise turbulence intensity
C_L	lift coefficient	u'	velocity fluctuations in the flow direction
C_p	pressure coefficient	v	kinematic viscosity of the fluid
$\mathbf{E}$	strain rate tensor	W	serration wavelength
H	tip-to-root distance of the serration		
h	half-height of the serration	α	angle of attack
Ma	Mach number	ε	oblique angle
U_0	inlet velocity	Q	Q-criterion
Re	Reynolds number	$\mathbf{\Omega}$	vorticity tensor

1. INTRODUCTION

It is known that the silent flight of owls are greatly associated with the serrated edges of their feathers (Lilley, 1998; Kroeger *et al.*, 1971). Recognizing this effect, attempts have been made to reduce aerodynamic noise by employing serrated trailing edge on the impeller blades of turbomachinery. As a successful example, Oerlemans *et al.* (Oerlemans *et al.*, 2009) reported promising average overall noise reductions of 3.2 dB on a 47-meter-long wind turbine (2.3 MW wind turbine from General Electric Company) blade with trailing edge serrations in acoustic field measurements, without adverse effect on the blade aerodynamic performance.

Aerodynamic noise produced near trailing edges of airfoils is strongly dependent on the flow Reynolds number Re. When airfoils operate at low-to-

moderate Reynolds numbers ($5.0 \times 10^4 < Re < 5.0 \times 10^5$), high levels of tonal noise are often produced at the airfoil trailing edges (Nakano *et al.*, 2006; Arcondoulis *et al.*, 2010). A number of researches concentrate on the mechanism of the noise reduction, mainly tonal noise, of employing serrated trailing edge within this range of Reynolds numbers.

Moreau *et al.* (Moreau *et al.*, 2013) experimentally studied the aerodynamic noise of a flat-plate with serrated trailing edges at $1.6 \times 10^5 < Re < 4.2 \times 10^5$. It was discovered that the serrations effectively suppressed the vortex shedding at the trailing edge, resulting in a high-frequency narrow band noise reduction up to 13dB. The mechanism was dominated by their influence on the hydrodynamic field at the source location. Larger reductions in noise were achieved with serrations with larger wavelength to height ratios. Chong *et al.* (Chong *et al.*, 2013) measured the tonal noise of NACA-0012 airfoils with serrated trailing edges at $1.6 \times 10^5 < Re < 4.2 \times 10^5$, in an acoustic tunnel with low turbulence intensity (0.5%). It was believed that the attenuations of the tonal noise were associated with the influence of the serrations on the T-S (Tollmien–Schlichting) wave and the separation bubble. The serrations weakened the instability of the T-S wave, and prevented the amplifications of the instability due to the separated boundary layer. Xu *et al.* (Xu *et al.*, 2012) confirmed suppression of the noise components of low-to-moderate frequencies, in the studies of NACA-0018 airfoils with serrated trailing edges at $Re=1.4 \times 10^5$ in a low-speed open jet wind tunnel. No noticeable influence on the aerodynamic performance of the airfoil was found.

The fact that very few numerical related researches can be found, is most likely due to the difficulty in implementing numerical methods with high fidelity, i.e., large eddy simulation (LES) or direct numerical simulation (DNS), in order to preserve the detailed flow information needed for the analysis of aeroacoustics. Han *et al.* (Han *et al.*, 2011) studied the flows over NACA-0012 airfoil with a sine wave shaped trailing edge, without angle of attack in a uniform stream at $Re=2.0 \times 10^5$, using LES with a dynamic subgrid scale model. Results indicated that a major source of aerodynamic noise was the quasi two-dimensional spanwise vortices near the trailing edge, and the wavy trailing edge reduced the pressure fluctuations near that region. Jones *et al.* (Jones *et al.*, 2012) conducted DNS studies of the flow around a NACA-0012 airfoil at $Re=5.0 \times 10^4$, employing an immersed boundary method to represent flat-plate trailing-edge extensions both with and without serrations. Trailing-edge noise reduction was derived in the range of Strouhal number $St > 5$. Flow analysis showed that the serrations broke up the larger turbulent structures convecting into the wake, and promoted the development of horseshoe vortices originating at the serrations themselves. More studies are needed for further clarification of the mechanism of noise reduction by serrated trailing edge with wider range

of Reynolds numbers.

This paper presents an analysis on the aerodynamic noise of airfoils with serrated trailing edges at $Re=1.6 \times 10^5$ based on embedded LES (ELES) flow simulations. The aeroacoustic analysis was performed by solving FW-H equations. The influence of the serrations on the flow structures associated with the trailing edge noise was discussed.

2. SIMULATION GEOMETRY

Most of aeroacoustic studies of airfoils concentrate on the NACA series and some turbomachinery dedicated airfoils. A NACA-0018 airfoil was chosen as baseline airfoil, with $18\%C$ maximum thickness, where the chord $C=80\text{mm}$.

Two types of serrated trailing edges have been used in previous references: a serrated flat-plate extension at the trailing edge of the baseline airfoil (Jones *et al.*, 2012), and a saw tooth serration attached to the truncated main body of the baseline airfoil (Chong *et al.*, 2013). Considering the influence of the serrations on the aerodynamic performance and the mechanical structural integrity in applications, and the requirements for the grid design in the numerical simulations, the latter arrangement was used in the present study.
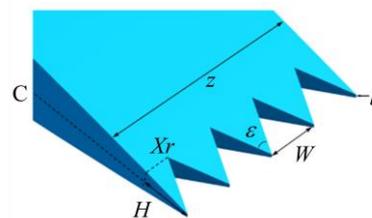
Fig. 1. Geometries of the serrated trailing edge.

Figure 1 shows the geometries of the serrated trailing edge. The dashed line C is the chord of the airfoil. On the spanwise plane passing through C, the tip-to-root distance of the serration is defined as $H=2h$. The half-height h represents the decrease in the effective chord length by the serration. Other geometrical parameters describing the serration include the oblique angle ε, and the width of a single saw tooth (serration wavelength) W, etc.

Airfoils with trailing edge serrations with two sets of geometric parameters, A1 and A2, were designed, as shown in Fig. 2 and Tab. 1. Their aerodynamic flow and noise were numerically studied against the baseline airfoil A0.

3. EMBEDDED LARGE EDDY SIMULATIONS

3.1 Computational Domain and Boundary Conditions

In order to reduce the computational load, an ELES method was utilized in this research, using

LES in areas in need of most attention, and Reynolds Averaged Navier-Stokes (RANS) simulations with SST *k-w* turbulence model in other areas (ANSYS Inc., 2011). As shown in Fig. 3, the whole computational domain can be divided into several parts. $R1$ and $R2$ are the two sub-domains, where RANS simulations were applied. L-out and L-in are two sub-domains using LES, with different computational grid densities. The leading edge of the airfoils locates at $0.3C$ from the origin of the coordinate system, along the direction of the main flows x. z is the spanwise direction. The distance from the inlet to the leading edge of the airfoils is about $5.2C$. The distance from the trailing edge of the airfoils to the outlet is about $5.8C$. The width of the computational domain in the spanwise direction $S = 0.2C$. The geometries of the domain relative to the chord C are shown in Tab. 2.

(a)

(b)

(c)
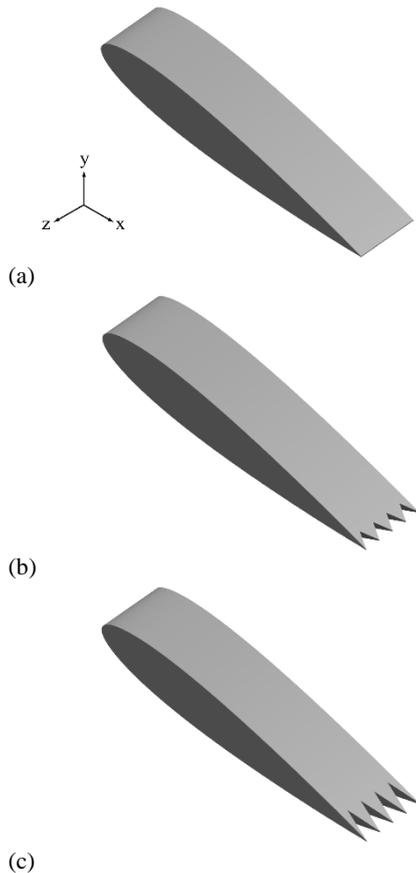
Fig. 2. Airfoil geometry (a) baseline A0, (b) and (c) airfoil with serrated trailing edges A1 and A2.

Table 1 Geometric parameters of trailing edge serrations

Serration types	H (mm)	X_r/C	W (mm)	ε (°)
A0	-	-	-	-
A1	4.0	0.95	4.0	53.13
A2	8.0	0.90	4.0	28.07

Table 2 Geometric parameters of the computational domain

Geometric parameters	$R1/C$	$L1/C$	$L2/C$
Value	4.0	1.5	2.5
Geometric parameters	$R2/C$	D/C	S/C
Value	4.0	3.0	0.2

According to references (Nakano *et al.*, 2006) and (Nakano *et al.*, 2007), at moderate Reynolds number, the most significant tonal noise of NACA-0018 airfoil occurs at the angle of attack $\alpha = 6^o$. Limited experimental data can be consulted for the velocity distributions of NACA airfoils at moderate Reynolds number. For the convenience of comparison, the baseline airfoil, the angle of attack, and the Reynolds number in our research were set as the same as in reference (Nakano *et al.*, 2006).

Velocity inlet and outflow outlet conditions were applied respectively. Inlet velocity was set as $U_0 = 30$ m/s, resulting a Reynolds number $Re = 1.6 \times 10^5$. Wall boundaries were specified at the top and bottom boundaries in y direction. Periodic conditions were set at along the spanwise direction. No-slip conditions were specified at the surface of the airfoils.

3.2 Computational Grid Design

Hexahedral grids were utilized in the entire computational domain. O-type topological structure was used in L-out region. L-in region, which contains the airfoils, adopted C-type topological structure. This setting ensures the high quality of the grids in the LES region, especially near the surface of the airfoils. The distribution of the number of grid cells of A0 is shown in Tab. 3. Grids in different regions were connected by interfaces, across which data exchanges were achieved through interpolations.

L-in region is of major concern in the calculations. In order to simulate the flows in the boundary layer with high accuracy, and capture the vortices with various sizes at the airfoil surface, wall-resolved LES method was applied. This requires a high grid resolution normal to the wall, i.e., $y^+ \leq 1$. At least three to five layers of nodes are also needed in the region of $0 < y^+ < 10$ (Sun *et al.*, 1994). Furthermore, high-resolution and medium-resolution LES have the requirements for grid resolutions in the direction of the flow, $x^+ \leq 50$ and $x^+ \leq 100$ respectively, and spanwise direction $z^+ \leq 12$ and $z^+ \leq 30$ respectively (Sun *et al.*, 1994). After trial and adjustment, the heights of the first layer grids in three directions were $\Delta y = 0.008$ mm, $\Delta x_{max} = 0.4$ mm, and $\Delta z = 0.25$ mm. This grid system satisfies $y^+ \leq 1$
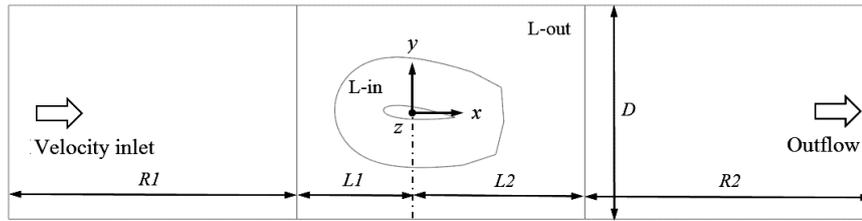
Fig. 3. Topology of the computational domain.

, $x^+ \leq 50$, $z^+ \leq 30$. And seven layers of grids existed in the range of $0 < y^+ < 10$. Thus, the grid system meets the requirement for medium-resolution LES. An instantaneous y^+ distribution on the surface of A2 can be seen in Fig. 5.

(a) L-in region

(b) L-out region
Fig. 4. Grids in LES region.

Table 3 Distribution of the number of grid cells of A0

Region	RANS	L-out	L-in
Number of Grids	0.31×10^6	0.77×10^6	6.6×10^6
Total number of grids	8.0×10^6		

3.3 Computational Settings

Since Mach number $Ma = U_0 / a = 0.088$, incompressible flow assumption can be applied. Double-precision data format was adopted in order to reduce truncation errors in calculations. The simulations were carried out in FLUENT 14.0 software.

Fig. 5. Instantaneous y^+ distribution on A2 surface.

Fig. 6. Locations of sections, indicated on A2.

The initial flow fields were derived by steady RANS simulations, with SST $k-\omega$ turbulence model. Unsteady flow simulations were then carried out until the stability of the lift and drag coefficients was achieved. Then LES module, with WALE (Wall-Adapting Local Eddy-viscosity) subgrid scale model was switched on in the LES region. Data collections for flow fields and sound sources were then performed until the ELES calculations reached a quasi-stable flow fields, i.e., the relative stabilization of lift and drag coefficients.

The size of time step was chosen as $ts = 2 \times 10^{-6}$, resulting in a flow distance of a fluid particle $7.5 \times 10^{-4} C$ in one time step. It was $1/5$ of the minimum size of the time scale in the flow. In each time step, it was observed that the residual errors in the continuum equation decreased by more than 10^3. Thus it was concluded that the time step was appropriate for capturing the unsteady flow characteristics in the flows. Second-order, second-order upwind, central difference, and second-order upwind discretization schemes were employed in pressure, momentum in RANS, momentum in LES, and the turbulence kinetics respectively. Second-order implicit scheme was used in time discretization.

The statistical data of the main parameters was sampled in the calculations. ELES calculations provided the data for sound sources, i.e., the time series of the pressure fluctuations at the locations of the sound sources near airfoil surface, in the following acoustic analogy analysis. Data sampling frequency was determined by the timescales of the unsteady flow process and the requirements for acoustic analogy analysis. In our research, data sampling was performed every 10 time steps, i.e., with frequency of $5.0 \times 10^4 \, \text{Hz}$. The total size of the sampling was $T = 0.03 \text{s}$, in which time the fluid particle had flowed pass a distance of $11.25C$.

4. AEROACOUSTIC ANALYSIS

It should be noted that noise determination through Lighthill analogy has been adopted for turbomachines, e.g., a pump (Christopher *et al.*, 2018). Since the airfoils in our research remained static, the FW-H equations could be simplified as Curle's equation (ANSYS Inc., 2011):

$$\frac{1}{c_0^2}\frac{\partial^2}{\partial t^2}[p'\text{H}(f)] - \nabla^2[p'\text{H}(f)] =$$
$$-\frac{\partial}{\partial x_i}[p_{ij}n_j|\nabla f|\delta(f)] + \frac{\partial^2}{\partial x_i x_j}[\mathbf{T}_{ij}\text{H}(f)]$$

$$(1)$$

where $\mathbf{T}_{ij} = \rho u_i u_j + p_{ij} - a_0^2 \rho \delta_{ij}$.

Due to the low Mach number in the studies, quadrupole sources terms in the acoustic analogy model were negligible. Thus the dipole source became the unsteady pressure near the airfoil surface. Then the far-field solutions for the Curle equation became (Zhan *et al.*, 2013):

$$p'(\mathbf{x},t) = -\frac{x_j}{4\pi|\mathbf{x}|c_0}\frac{\text{d}}{\text{d}t}\left\{\iint_{\partial V}\frac{pn_j}{r}\text{d}^2\mathbf{y}\right\}_{t-r/c_0} \quad (2)$$

where $\mathbf{x}$ is the position vector of the sound pressure monitoring point, t is the launch time at the sound source, ∂V is the solid boundaries, r is the is the distance between the monitoring point to the sound source, and $\mathbf{y}$ is the position vector of the sound source.

The time-domain sound pressure signals were derived through Eq. (2) after the retrieving the flow field data from CFD analysis. The reference sound pressure was set as $2.0 \times 10^{-5} \, \text{Pa}$.

5. RESULTS AND DISCUSSIONS

5.1 General Features of the Flow

The general features of the flow over the baseline airfoil A0, including the time-averaged velocity and turbulence intensity in the flow direction are presented in this part. Similar features can be found in the cases of A1 and A2. Figure 6 shows the locations of the two sections used for displaying flow features, indicated on A2.

Figure 7 shows the distribution of the time-averaged velocity amplitude around A0, normalized with freestream inlet velocity $U_0 = 30 \, \text{m/s}$. It can be seen that at the angle of attack $\alpha = 6^\circ$, the stagnation point is located on the pressure side of the leading edge. A semi-circular zone with relatively high velocity amplitude occurs from the suction side of the leading edge.

Figure 8 shows the streamwise turbulence intensity distribution around A0 on $Z\text{m}$, which is defined as $T_u = \frac{1}{U_0}\text{RMS}\,u'$, where u' is the velocity fluctuations in the flow direction. Generally higher intensity can be seen on the suction side of the airfoil. Strong intensity area (indicated as the color red) locates at $0 < x < 0.2$. The thickness of the area with relatively strong intensity increases along the flow direction on the suction side. Weak turbulence intensity is observed on the pressure side, except at the trailing edge, where an area of strong intensity occurs.
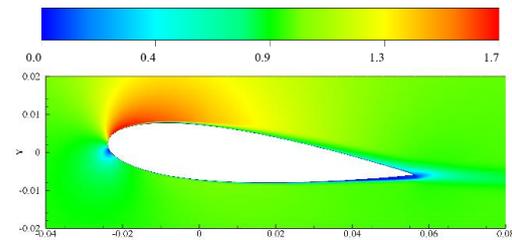
Fig. 7. Time-averaged velocity amplitude of case A0 (on $Z\text{m}$).
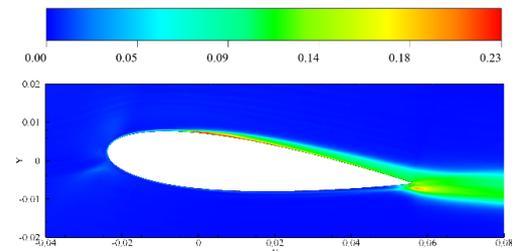
Fig. 8. Streamwise turbulence intensity of case A0 (on $Z\text{m}$).

5.2 Time-Averaged Pressure Coefficients

The pressure coefficient is defined as

$$C_p = \frac{p - p_r}{\frac{1}{2}\rho U_0^2} \quad (3)$$

where p is the wall pressure, the reference pressure p_r is defined as the area-weighted average static pressure on the corresponding section in the flow field.

Figure 9 illustrates the comparison of the distribution of the pressure coefficient between time-averaged results from ELES and the experiments (Nakano *et al.*, 2006). It can be seen

that the simulation results have a good agreement with the experiments.
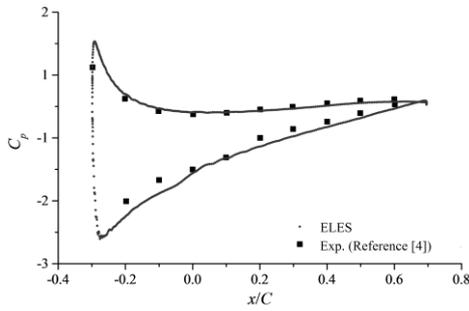
Fig. 9. Comparison of pressure coefficient between time-averaged ELES and experiments (A0).
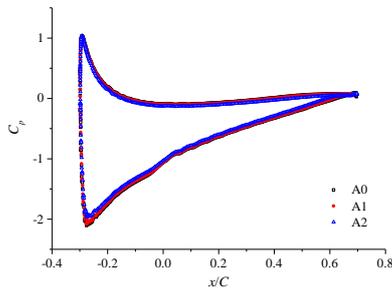
(a)
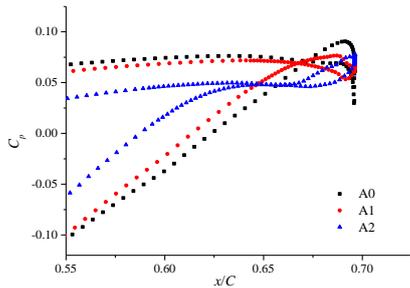
(b)

Fig. 10. Pressure coefficients of airfoils (on Zm).

The calculated time-averaged pressure coefficients on Zm of all three cases can be seen in Fig. 10. Note that Zm passes through the tip of the saw tooth in cases A1 and A2. Very similar distribution are observed in all cases. The smallest absolute values of the pressure coefficients on both suction and pressure sides occur in case A2. The existence of the saw tooth causes an overtaking of the pressure on suction side over pressure side, at the very end of the trailing edge.

The calculated time-averaged pressure coefficients on Zr of all three cases can be seen in Fig. 11. Note that Zr passes through the root of the saw tooth in cases A1 and A2. The existence of the saw tooth does not have a significant influence on the distribution nearby.

5.3 RMS Pressure Fluctuations.

In order to compare the influence of two types of serrations on the boundary layer and the near field pressure fluctuations, the distribution of RMS

pressure fluctuations, normalized by $\frac{1}{2}\rho U_0^2$, have been analyzed.
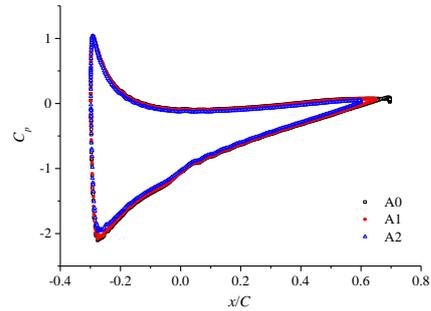
Fig. 11. Pressure coefficients of airfoils (on Zr).

(a) A0
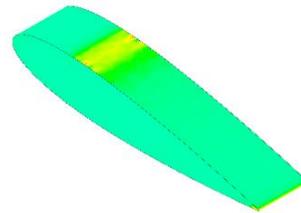
(b) A1
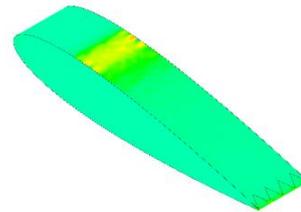
(c) A2
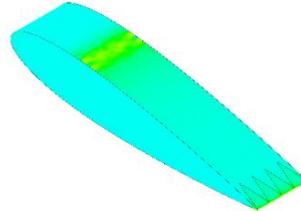
Fig. 12. RMS pressure fluctuations on airfoil surface.

As shown in Fig. 12, a band region of high RMS pressure fluctuations exists $C/3$ away from the leading edges of the airfoils on the suction side, corresponding to the area of high turbulence intensity in Fig. 8. This indicates a possible separation bubble at this location. Another region of high RMS pressure fluctuations occurs at the trailing edge. Comparing the reduction in pressure fluctuations observed only near trailing edge by sine wave shaped trailing edge in reference (Han *et al.*, 2011), in our research with two types of saw tooth serrations, case A2 possesses overall lower RMS pressure fluctuations on the airfoil surface than A0 and A1, which can be distinguished by the coloring.

5.4 3D Vortex Structures

Q-criterion was chosen for vortex visualizations in our research, defined as $Q = \frac{1}{2}(\|\mathbf{\Omega}\|^2 - \|\mathbf{E}\|^2)$, where $\mathbf{\Omega}$ and $\mathbf{E}$ are the vorticity tensor and the strain rate tensor respectively. The area in which $Q > 0$ can be deemed as vortex core area, i.e., the movements of the fluid are dominated by rotations (Tong *et al.*, 2009).

(a) A0

(b) A1

(c) A2
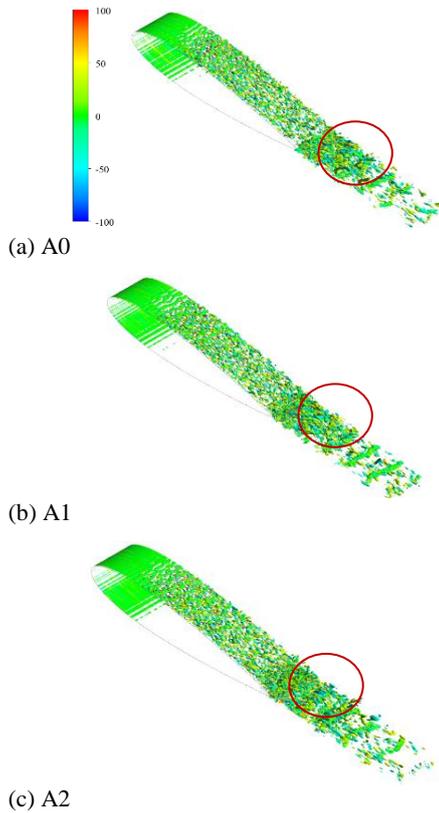
Fig. 13. $Q^* = 200$ **isosurfaces around airfoils.**

The instantaneous vortex structures around the three airfoils are shown in Fig. 13, where $Q^* = Q / F^2$, $F = U_0 / C$. Colors indicate the normalized magnitude of the streamwise vorticity $\omega_x^* = \omega_x / F$. Small vortex structures occur $C/3$ away from the leading edges of the airfoils on the suction side in all three cases. Near the trailing edge vortex structures become denser, and larger scale vortices are developed in the downstream wake. The distributions of the vortex structures, and the streamwise vorticity are similar in all three cases. Slightly denser and smaller vortex structures after the trailing edges occur in cases A1 and A2.

5.5 Unsteady Force Characteristics

The lift and drag coefficients are defined as

$$C_L = \frac{F_L}{\frac{1}{2}\rho U_0^{\,2} CL} \tag{4}$$

$$C_D = \frac{F_D}{\frac{1}{2}\rho U_0^{\,2} CL} \tag{5}$$

respectively. In our research, the chords of A1 and A2 are calculated as $C' = C - h$, considering the influence of the saw tooth serrations to the effective surface area of the airfoils.

(a)   Time series
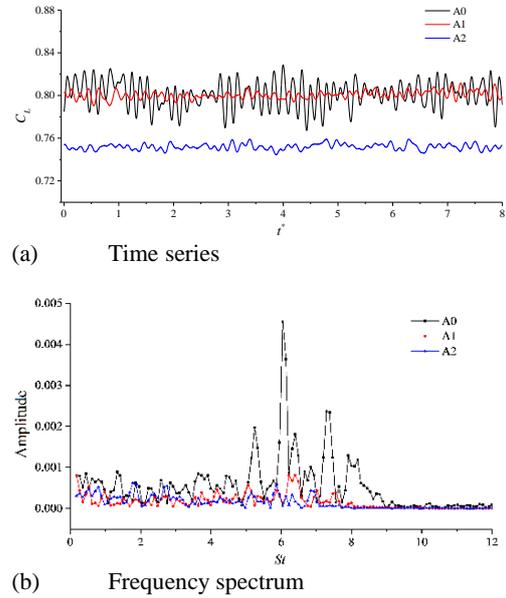
(b)   Frequency spectrum
Fig. 14. Unsteady lift coefficients.
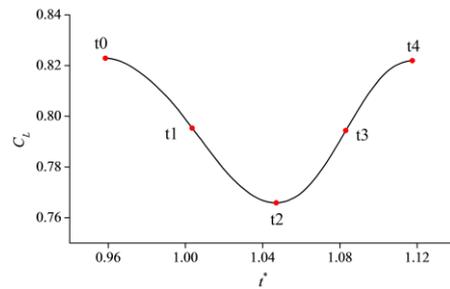
Fig. 15. One typical oscillating cycle of C_L of A0.

Figure 14 provides the unsteady lift coefficients in all three cases. The non-dimensional time $t^* = t / (C / U_0)$. It can be observed that airfoils A0 and A1 have similar time-averaged lift coefficient. Time-averaged lift coefficient of A2 is about 0.5 smaller than A0 and A1. Significant periodicity exists in the lift coefficient of the baseline airfoil A0, indicating the presence of flow structures with substantial periodical pressure fluctuations, e.g., the periodic shedding of vortices near the trailing edge, etc. In contrast, the variations of lift coefficients of A1 and A2 are less volatile, with no significant periodicity. Frequency analysis shows that a peak appears in the vicinity of $St = 6.04$ in case A0, where the Strouhal number is defined as $St = f / (U_0 / C)$. This peak corresponds to a frequency of about 2270Hz, which is close to the tonal noise frequency (2000~2100Hz) observed in

(a) streamlines and velocity   (b) spanwise vorticity
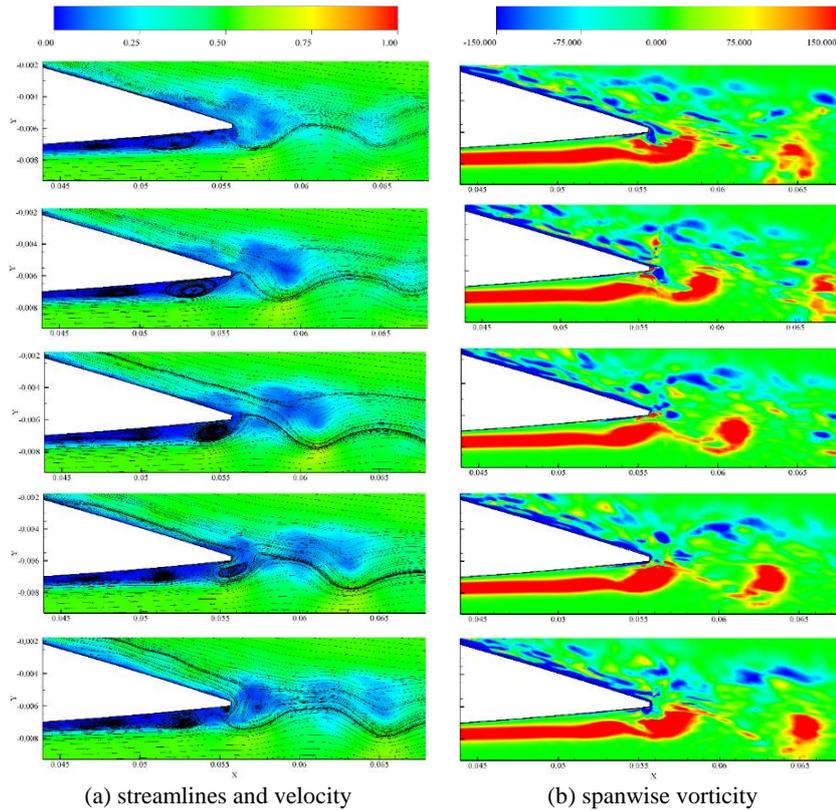
Fig. 16. Instantaneous flows near trailing edge of A0 (on Zm), top to down: t0~t4.

experiments (Nakano *et al.*, 2006; Nakano *et al.*, 2007). This peak disappears in cases A1 and A2, indicating a destruction in the periodicity of the pressure variations on the airfoil surface. Similar frequency spectra of the unsteady drag coefficients for the three cases are derived, with a peak at 2270Hz with A0.

5.6 Unsteady Flow Field

This subsection investigates the instantaneous flow fields at typical times around three airfoils.

In the case of A0, a major frequency 2270Hz of lift coefficients was captured, as illustrated in 5.5, corresponding to a period of 4.4×10^{-4}s. Five typical times in one typical oscillating cycle of C_L of A0, shown in Fig. 15, were chosen for instantaneous flow analysis.

Figure 16 shows the instantaneous flows over A0 at t0~t4. Column (a) shows the streamlines, colored with the amplitude of normalized velocity amplitudes. Column (b) shows the normalized spanwise vorticity. As shown in the figure, at t0, a vortex structure with positive vorticity is leaving the trailing edge at $0.055 < x < 0.059$ on the pressure side of the trailing edge. From t1 to t3, this structure moves towards downstream, with its shape shifting. A new structure occurs at the same location. At t4, the first vortex structure moves to $x = 0.065$, and the second structure starts to shed. The distance between the two vortices is about 0.008 m，i.e.，$0.1C$. After one period, the

flow fields recovers to that of t0. It can be concluded that the periodic variation of the lift, drag, and the pressure field around the airfoil, are caused by the periodic vortex shedding at the pressure side of the trailing edge.

As illustrated in 5.5, the variations of the aerodynamic forces of airfoil A1 have smaller oscillating amplitudes, and much less periodicity, compared with A0. A quasi-period of lift coefficient oscillation, with the same length of time period with that of A0, was chosen for analysis (Fig. 17).
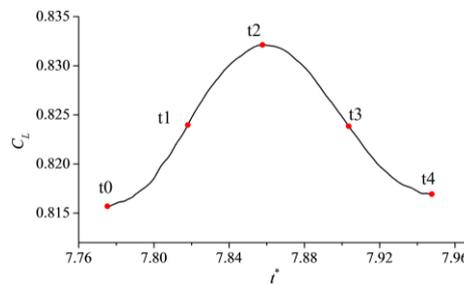
Fig. 17. One oscillating quasi-cycle of C_L of A1.

Figure 18 provides the flows of A1. At time t1 to t2, the vortex shedding occurs at the pressure side of the trailing edge. Then the vortex breaks down to much smaller structures while moving towards downstream (t3 and t4). No concentrated vortex structure can be observed at about $x = 0.06$ at t4.

(a) streamlines and velocity   (b) spanwise vorticity
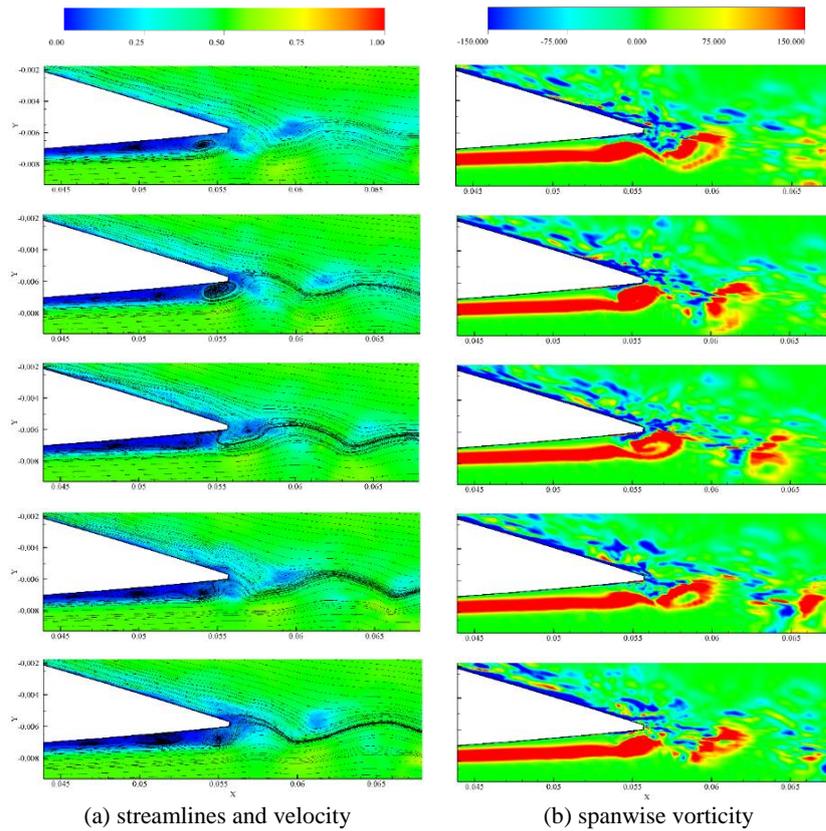
Fig. 18. Instantaneous flows near trailing edge of A1 (on Zm), top to down: t0~t4.

Similar to the case A1, a quasi-period was chosen for analysis (Fig. 19). Note that the oscillation of the lift coefficient is much smaller than A0 and A1. A much thinner area of reverse flow can be observed (Fig. 20). The breakdown of the shedded vortex is even faster than in the case A1.

Comparing the movements of the vortex structures in the three cases, it can be seen that, during the period that the vortex moves about 0.0005m: the vortex in A0 rotates about 60° (t0-t2), without breaking down; the vortex in A1 rotates about 10° (t2-t4), and breaks down completely; the vortex in A2 rotates about 90° (t0-t2), and breaks down. This indicates that the longer saw tooth at the trailing edge of A2 influences the flows near the pressure side of the trailing edge, and destroys the periodicity of the variation of the vortex structure. Since the trailing edge noise is strongly related to the pressure fluctuations near the airfoil trailing edge, it is implied that the radiated noise of A1 and A2 are weaker than that of A0. In order to understand the influence of the saw tooth to the local flow field, it is necessary to perform a further analysis on the boundary layer and wake development near the trailing edges, and the flow structures inside the saw tooth serrations.

5.7 Flow Profiles Near Trailing Edge

Four and five locations at the trailing edge and in the wake are chosen for flow profile analysis

respectively (Fig. 21).

Figure 22 shows the time-averaged and RMS velocity profiles near trailing edge of the three airfoils. At T1 (streamwise location of saw tooth root on A2), flow separation on pressure side is seen. At T2, turbulence fluctuations of the velocity appear near surface of A0 and A2. At T3, the reverse flow velocity of A2 exceeds that of A0 and A1. In the separation zone, the turbulence intensity of A0 and A2 are stronger than that of A1. Note that the location of saw tooth root of A1 is in the middle of T2 and T3. At T4, it can be observed that the turbulence intensity of A2 is slightly higher. But the reverse flow disappears. It can be concluded that the shear layer after separation at the trailing edge surface of A2 is thinner than that of A0 and A1.
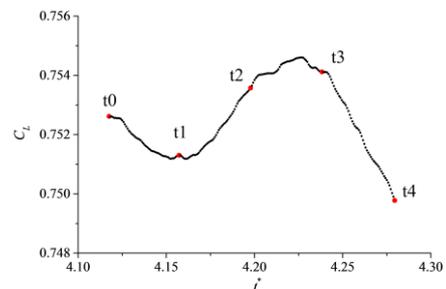
Fig. 19. One oscillating quasi-cycle of C_L of A2.

(a) streamlines and velocity   (b) spanwise vorticity
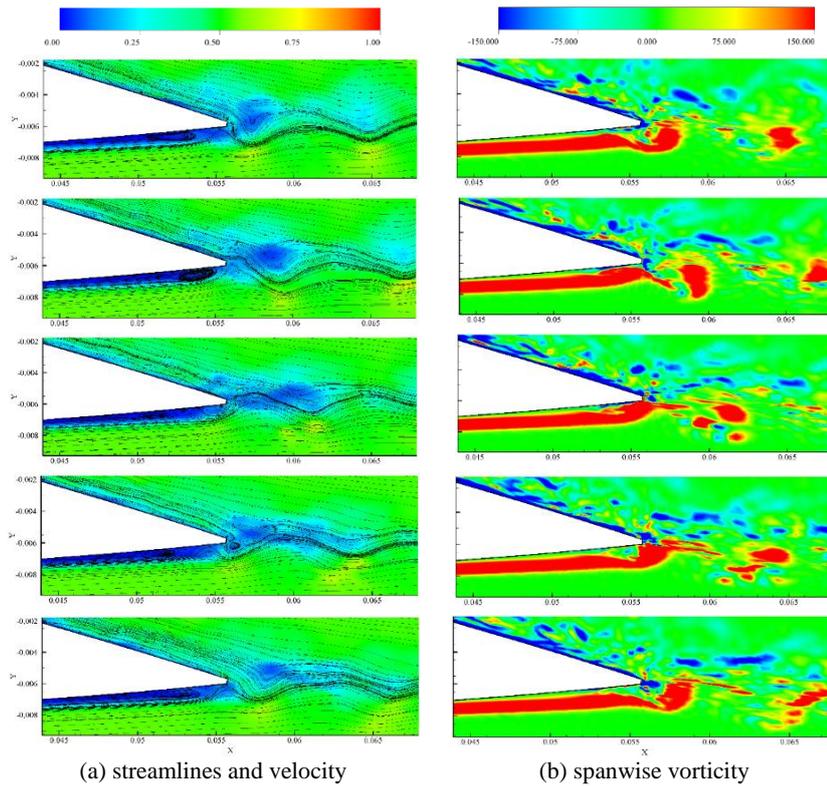
Fig. 20. Instantaneous flows near trailing edge of A2 (on Zm), top to down: t0~t4.

Flow profiles in the wake of the three cases can be seen in Fig. 23. At W1, which is near the end of the trailing edge, the profiles indicate that the shear layers of the pressure side are thinner than that of the suction side. Slightly higher turbulence intensities exist in the pressure side. From W2~W4, the pressure gradients in the shear layers, as well as the turbulence intensity, decrease. At W5, $0.3C$ away from the trailing edge, the characteristics of the wake flow are very weak. Comparing the three cases, highest velocities can be observed in the shear layer on the pressure side of A2. Before W3, strongest turbulence intensity exists in the shear layer of A2. While outside the shear layer, strongest turbulence intensity exists in the wake of A0, weakest in that of A2.
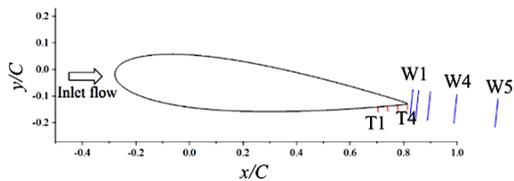
Fig. 21. Locations for velocity profile analysis (Zm).

Table 4. Noise monitoring points near airfoils (Zm)

Monitoring points	R1	R2	F1	F2
x (m)	0	0	0.056	0.056
y (m)	0.12	-0.12	0.4	-0.4

5.8 Flows in the Saw Tooth Serrations

As seen in Fig. 6, Zr section passes through the roots of the saw tooth serrations of A1 and A2. Figure 24 shows the time-averaged streamlines near the saw tooth serrations, with background colored with the magnitude of the local velocity. It can be observed that, near the pressure side of the trailing edge of the baseline airfoil A0, reverse flow vortex exists. The fluid on the suction side flows around the end of the trailing edge to the pressure side. Within the area of the saw tooth, and the low velocity area on the pressure side, A1 has a relatively complex vortex structure. Clockwise flows inside the saw tooth indicate that a higher momentum is reached in the flows on the suction side. Clockwise flows occur in A2 as well, with a similar location of the vortex center compared with A1. Flows from the suction side to the pressure side can be observed near the root of the saw tooth. A smallest area of reverse flow appears on the pressure side of A2.

The distributions of spanwise vorticity near the saw tooth serrations in all three cases are shown in Fig. 25. The vortices with negative vorticity appear at the suction side near the trailing edge, and breaks down to structures with much smaller scales very quickly. Area with strongest vorticities appears near the trailing edge and in the wake of A2. No vorticities are generated within the saw tooth serrations.

5.9 Aeroacoustic Noise

For the purpose of airfoil noise analysis, four
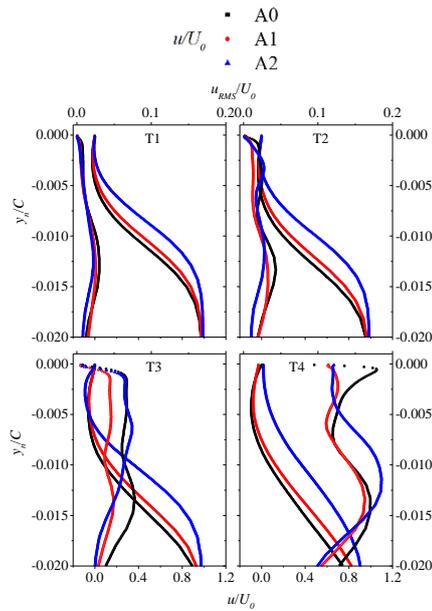
Fig. 22. Flow profiles at trailing edge.
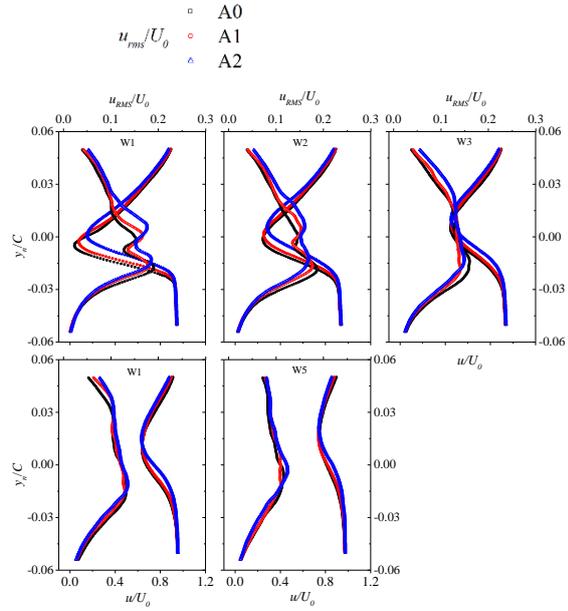
Fig. 23. Flow profiles in the wake.
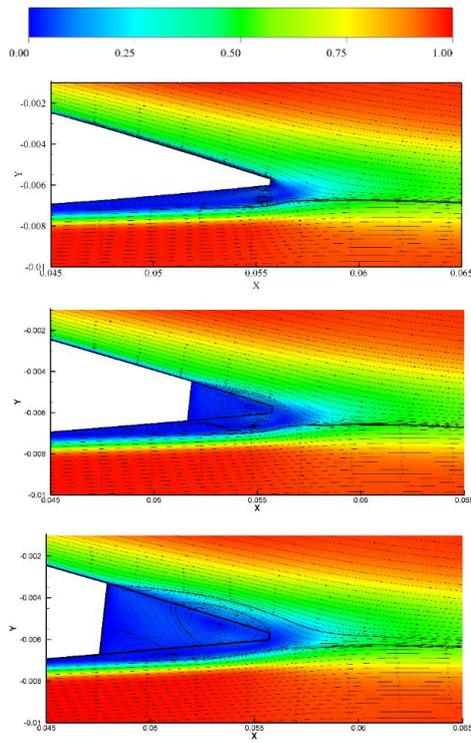
Fig. 24. Time-averaged streamlines and velocity (Zr), top to bottom: A0, A1, A2.
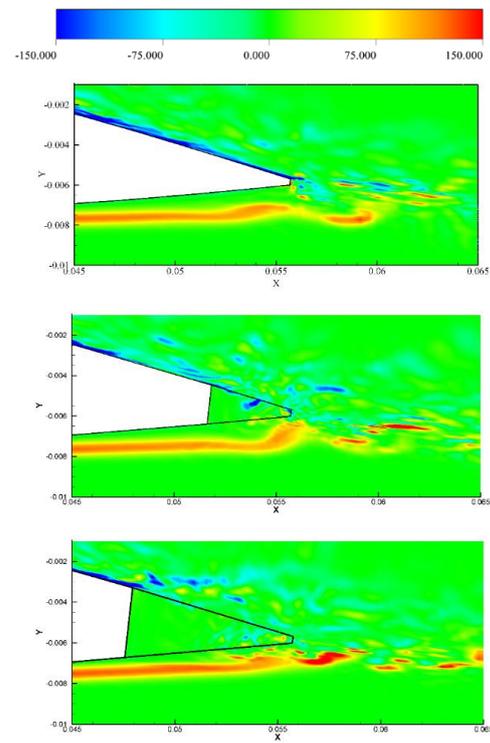
Fig. 25. Spanwise vorticity near saw tooth (Zr), top to bottom: A0, A1, A2.

monitoring points near the airfoils have been chosen. Points R1 and R2 are located at the up and bottom positions 1.5C away from the center of the airfoils respectively. Points F1 and F2 are located at the up and bottom positions 5C away from the trailing edge of the airfoils respectively. Another thirty-seven monitoring points are located on a circle, centered at the trailing edge of the airfoils, with 10C radius, in order to acquire the directivity

pattern of the far field sound pressure level.

As illustrated previously, the ELES calculations in this research provide the required information of boundary sound sources. By solving FW-H equation, the fluctuating pressure signals at the monitoring points in the time domain can be obtained. The frequency domain characteristics can be derived with FFT analysis. The intensity of the

sound pressure is measured with sound pressure level

$$SPL(f_n) = 10\log(\frac{p'^2(f_n)}{p^2_{ref}}) \qquad (6)$$

where $p'(f_n)$ is the sound pressure of frequency f_n in the spectrum. The reference sound pressure is $p_{ref} = 2 \times 10^{-5}$ Pa. The overall sound pressure level (OASPL) is defined as

$$OASPL = 10\log(\frac{\int p'^2(f_n)\,\mathrm{d}f}{p^2_{ref}}) \qquad (7)$$

Figure 26 illustrates the frequency spectrum at R1. The resolution of the frequency analysis is 33.3Hz, due to the limitation of the sampling. It is observed that a peak of around 2270Hz appears in case A0, which is consistent with the fluctuations of the lift and drag coefficients, and the shedding of the trailing edge vortex. This frequency is also close to the results of trailing edge vortex shedding by PIV, and tonal noise frequency by microphone measurements (2000~2200Hz) (Nakano *et al.*, 2006; Nakano *et al.*, 2007). With increasing size of the saw tooth serrations, the amplitude of this frequency component decreases. At most frequencies, the sound pressure levels of A1 and A2 are slightly lower than that of A0. Similar results are seen at monitoring points R2, F1, and F2.
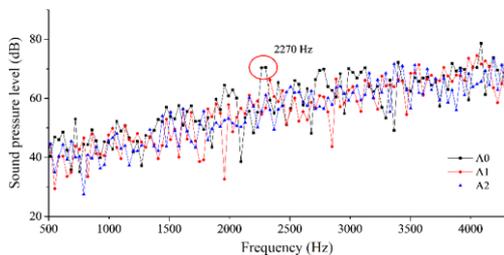
Fig. 26. Frequency spectrum of sound pressure level at R1.
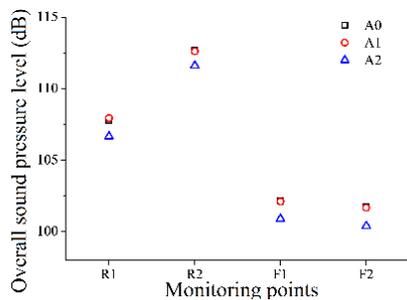
Fig. 27. Overall sound pressure level.

As illustrated in Fig. 27, the OASPL at different monitoring points in case A0 and A1 have similar amplitudes. The OASPL in case A2 is around 1.5dB lower than that of A0 and A1. Notice that R2 is close to the pressure side trailing edge, which has the highest OASPL. This indicates that the locations of the sound sources are near the pressure side of the trailing edges.

Figure 28 shows the directivity pattern of the far field sound of all three cases, centered with the trailing edge of the airfoils. It is observed that the strongest noise occurs in the direction of about $84° - 264°$ perpendicular to the trailing edge, which is about 30dB stronger than in streamwise direction ($174° - 354°$). The far field radiations of airfoil A2 in all directions are weaker than that of A0 and A1.
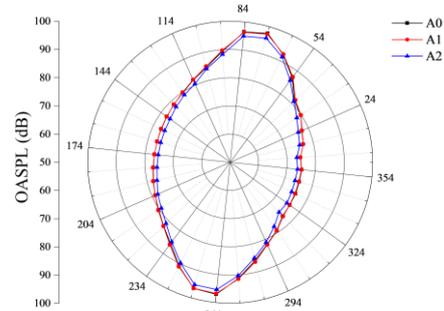
Fig. 28. Directivity of the far field sound.

6.   CONCLUSIONS

This paper presents the numerical analysis on the aerodynamic flows and noise of airfoils with serrated trailing edges (baseline NACA-0018 airfoil) at low to moderate Reynolds number.

Time-averaged results of medium resolution ELES indicate that, the saw tooth serrations have weak influence of the time-averaged flow fields upstream. The longer saw tooth serrations (case A2) decrease the amplitudes of the pressure fluctuations near airfoil surfaces.

The unsteady lift and drag coefficients of the baseline airfoil A0 have a peak at about 2270Hz, which is close to the tonal noise frequency observed in previous references. This frequency is consistent with the vortex shedding frequency at the pressure side of trailing edge of A0. In cases A1 and A2, the vortex structure breaks down quickly after shedding.

Under the flow conditions studied in this research, the longer saw tooth serrations (A2) changed the flow fields near the trailing edge, which provides the potential of suppressing the tonal noise. Predictions based on acoustic analogy indicate that the longer saw tooth serrations decreases the overall sound pressure levels.

REFERENCES

ANSYS Inc. (2011). ANSYS Help 14.0: Fluent theory guide.

Arcondoulis, E. J. G. and C. J. Doolan (2010). A review of trailing edge noise generated by airfoils at low to moderate Reynolds number. *Acoustics Australia* 38(3), 129-133.

Chong, T. P. and P. F. Joseph (2013). An experimental study of airfoil instability tonal noise with trailing edge serrations. *Journal of Sound and Vibration* 332(24), 6335-6358.

Christopher, S., S. Q. Yuan, J. Pei, G. X. Cheng and Y. Y. Wang (2018). Study of flow induced noise in vertical inline pump using Lighthill analogy. *MATEC Web of Conferences* 172, 01010.

Han, C., T. Omori and T. Kajishima (2011). Numerical simulation of turbulent flow past a serrated airfoil. *ASME-JSME-KSME 2011 joint fluids engineering conference. Am Soc Mech Eng*, 1185-1194.

Jones, L. E. and R. D. Sandberg (2012). Acoustic and hydrodynamic analysis of the flow around an aerofoil with trailing-edge serrations. *Journal of Fluid Mechanics* 706, 295-322.

Kroeger, R. A., H. D. Gruschka and T. C. Helvey (1971). Low speed aerodynamics for ultra-quiet flight. *AFFDL/TR*, 971-975.

Lilley, G. M. (1998). A study of the silent flight of the owl. *4th AIAA/CEAS Aeroacoustics Conference, Aeroacoustics Conferences* 2340, l-6.

Moreau, D. J. and C. J. Doolan (2013). Noise-reduction mechanism of a flat-plate serrated trailing edge. *AIAA Journal* 51(10), 2513-2522.

Nakano, T., N. Fujisawa and S. Lee (2006). Measurement of tonal-noise characteristics and periodic flow structure around NACA0018 airfoil. *Experiments in Fluids* 40(3), 482-490.

Nakano, T., N. Fujisawa, Y. Oguma, Y. Takagi and S. Lee (2007). Experimental study on flow and noise characteristics of NACA0018 airfoil. *Journal of Wind Engineering and Industrial Aerodynamics* 95(7), 511-531.

Oerlemans, S., M. Fisher, T. Maeder and K. Kögler (2009). Reduction of wind turbine noise using optimized airfoils and trailing-edge serrations. *AIAA Journal* 47(6), 1470-1481.

Sun, X. F. and S. Zhou (1994). Aero-acoustics. *National Defense Industry Press*, Beijing.

Tong, B., X. Yin and K. Zhu (2009). Vortex motion theory (2nd Ed.), *University of Science and Technology of China Press*, Hefei.

Xu, Y. and X. Li (2012). An experiment study of the serrated trailing edge noise. *Acta Aerodynamica Sinica* 30(1), 120-124.

Zhan, F. and J. Xu (2013). Virtual.Lab Acoustics: Acoustic simulation- from entry to the master. Xi'an, *Northwestern Polytechnical University Press*.